

Two Nearby 10-Billion Solar Mass Black Holes

Nicholas J. McConnell¹, Chung-Pei Ma¹, Karl Gebhardt², Shelley A. Wright¹, Jeremy D. Murphy², Tod R. Lauer³, James R. Graham^{1,4} and Douglas O. Richstone⁵

October 3, 2011

¹Department of Astronomy, University of California, Berkeley, California 94720, USA. ²Department of Astronomy, University of Texas, Austin, Texas 78712, USA. ³National Optical Astronomy Observatory, Tucson, Arizona 85726, USA. ⁴Dunlap Institute for Astronomy and Astrophysics, University of Toronto, Ontario, Canada. ⁵Department of Astronomy, University of Michigan, Ann Arbor, Michigan 48109, USA.

Observational work conducted over the last few decades indicates that all massive galaxies harbor supermassive black holes at their centers. Although the luminosities and brightness fluctuations of quasars in the early Universe suggest that some are powered by black holes containing more than 10 billion solar masses¹, the remnants of these objects have not been found in the nearby Universe. For over three decades, the giant elliptical galaxy Messier 87 has hosted the most massive known black hole, with a mass of 6.3 billion solar masses^{2,3}. Here we report the discovery of a 9.7 billion solar mass black hole in NGC 3842, a brightest cluster galaxy at the center of a galaxy cluster 321 million light years away, and a black hole of comparable or larger mass in NGC 4889, the brightest galaxy in the Coma cluster 336 million light years away. The black holes in NGC 3842 and NGC 4889 are significantly more massive than predicted by linearly extrapolating the widely-used correlations between black hole mass and stellar velocity dispersion or bulge luminosity of the host galaxy⁴⁻⁸. While these correlations remain useful for less massive elliptical galaxies, our new measurements suggest that different evolutionary processes influence the growth of the largest galaxies and their black holes.

Empirical scaling relations between black hole mass (M_{BH}), galaxy bulge velocity dispersion (σ), and luminosity (L) are commonly used to estimate black hole masses, since most galaxies lack direct measurements of M_{BH} . Estimates of the number density of black holes in a given mass range thus depend upon the empirically determined slope of the $M_{\text{BH}} - \sigma$ and $M_{\text{BH}} - L$ relations over an appropriate range of galaxy masses. Directly measuring M_{BH} using the kinematics of stars or gas in the vicinity of the black hole is particularly difficult at the highest galaxy masses, because massive galaxies are rare and their typical distances are large. The most massive galaxies are typically Brightest Cluster Galaxies (BCGs), giant ellipticals that reside near the centers of galaxy clusters.

We have obtained high-resolution data of NGC 3842 and NGC 4889, using the instruments GMOS⁹ at the 8-meter Gemini North telescope and OSIRIS¹⁰ at the 10-meter Keck 2 telescope. NGC 3842 is the BCG of Abell 1367, a moderately rich galaxy cluster. NGC 4889 is the BCG of the Coma cluster (Abell 1656), one of the richest nearby galaxy clusters. We have targeted these two galaxies because they have relatively high central surface brightness and lie at an accessible distance for high-resolution studies. To constrain stellar kinematics at large radii, we observed the same galaxies with VIRUS-P¹¹ at the 2.7-meter Harlan J. Smith telescope. GMOS, OSIRIS, and VIRUS-P are all integral field spectrographs, which record spectra at multiple positions in a two-dimensional spatial array. The stellar luminosity distribution of each galaxy is provided by surface photometry from the Hubble Space Telescope and ground-based telescopes

^{12,13}.

We have measured the distribution of stellar velocities at 82 different locations in NGC 3842. The stellar velocity dispersion in NGC 3842 is between 270 and 300 km s⁻¹ at large radii and rises in the central 0.7 arcseconds ($r < 330$ pc), peaking at 326 km s⁻¹ (Figures 1-2). The localized central region of high velocity dispersion is a qualitative indicator of the presence of a supermassive black hole. We have determined the mass of the black hole by constructing a series of orbit superposition models¹⁴. Each model assumes a black hole mass, stellar mass-to-light ratio, and dark matter profile, and generates a library of time-averaged stellar orbits in the resulting gravitational potential. The model then fits a weighted combination of orbital line-of-sight velocities to the set of measured stellar velocity distributions. The goodness-of-fit statistic χ^2 is computed as a function of assumed M_{BH} and stellar mass-to-light ratio, M_*/L . Using our best-fitting model dark matter halo and data from GMOS and VIRUS-P, we measure a black hole mass of $9.7 \times 10^9 M_{\odot}$, with a 68% confidence interval of $7.2 - 12.7 \times 10^9 M_{\odot}$. Models with no black hole are ruled out at the 99.996% confidence level ($\Delta\chi^2 = 17.1$). We find a stellar mass-to-light ratio, M_*/L , of $5.1 M_{\odot}/L_{\odot}$ in R band, with a 68% confidence interval of $4.4 - 5.8 M_{\odot}/L_{\odot}$.

We have measured stellar velocity distributions in NGC 4889 with the integral-field spectrograph on GMOS, and have combined our measurements with published long-slit kinematics at larger radii¹⁵. The largest velocity dispersions in NGC 4889 are located across an extended region on the east side of the galaxy. The stellar orbits in our models are defined to be symmetric about the galaxy center, so we constrain M_{BH} by running separate trials with velocity profiles from four quadrants of the galaxy. The best-fit black hole masses from the four quadrants range from $9.8 \times 10^9 M_{\odot}$ to $2.7 \times 10^{10} M_{\odot}$.

Although no single model is consistent with all of the observed kinematic features in NGC 4889, we can define a confidence interval for M_{BH} by considering the most extreme confidence limits from the cumulative set of models. The corresponding 68% confidence interval is $0.6 - 3.7 \times 10^{10} M_{\odot}$. We adopt a black hole mass of $2.1 \times 10^{10} M_{\odot}$, corresponding to the midpoint of this interval.

The strongest constraints on the black hole masses in NGC 3842 and NGC 4889 come from GMOS data, which have high signal-to-noise at a seeing-limited spatial resolution of 0.4 arcseconds (200 pc). In comparison, the black hole dominates the galaxy's gravitational potential within a radius of 570 pc for NGC 3842, and 720 pc for NGC 4889. We describe data from other instruments in Supplementary Information; these data confirm our measurements with GMOS and provide additional constraints for models of the galaxies.

Figure 3 shows the $M_{\text{BH}} - \sigma$ and $M_{\text{BH}} - L$ relations, using data compiled from publications through August 2011, plus our measurements of NGC 3842 and NGC 4889. Tabulated data with references and our fits to $M_{\text{BH}}(\sigma)$ and $M_{\text{BH}}(L)$ are provided as Supplementary Information. The most widely used form for both relations is a power law with constant index. The relationship between σ and L , however, flattens at high galaxy

masses, and constant-index power laws for $M_{\text{BH}} - \sigma$ and $M_{\text{BH}} - L$ deliver contradictory predictions for M_{BH} in this mass range¹⁶. Direct measurements of M_{BH} in higher mass galaxies will compel the revision of one or both of $M_{\text{BH}} - \sigma$ and $M_{\text{BH}} - L$ relations.

Although NGC 3842 hosts a black hole more massive than any previously detected, its average velocity dispersion of 270 km s^{-1} within one effective radius ranks only 14th among 65 galaxies with direct measurements of M_{BH} . Its luminosity ranks 5th in this sample of galaxies, exceeded only by other BCGs. Based on σ and L in NGC 3842, the $M_{\text{BH}} - \sigma$ and $M_{\text{BH}} - L$ relations would predict $M_{\text{BH}} = 9.1 \times 10^8 M_{\odot}$ and $2.5 \times 10^9 M_{\odot}$, respectively. Similarly, the predicted black hole mass for NGC 4889 are $3.3 \times 10^9 M_{\odot}$ and $4.5 \times 10^9 M_{\odot}$ from σ and L , respectively. These predictions fall below our direct measurements of M_{BH} , by amounts greater than the intrinsic scatter in the $M_{\text{BH}} - \sigma$ and $M_{\text{BH}} - L$ relations⁸. In comparison, recent M_{BH} measurements based on gas kinematics in two other BCGs lie within 1.5 standard deviations of our revised $M_{\text{BH}} - \sigma$ and $M_{\text{BH}} - L$ relations¹⁷, while the measurement in NGC 1316, the Fornax BCG, falls significantly below the $M_{\text{BH}} - L$ relation¹⁸. The high scatter indicated by this collection of measurements reveals large uncertainties in the standard practice of using galaxy velocity dispersions or luminosities as proxies for the central black hole mass in giant elliptical galaxies and their predecessors.

Several BCGs within 200 Mpc are at least twice as luminous as NGC 3842, and three times as luminous as M87, the host of the most massive known black hole prior to this work. In spite of their extreme luminosities, BCGs have similar velocity dispersions to the most massive group and field elliptical galaxies. Yet the most massive black holes are found predominantly in BCGs (see Figure 3). How galaxies are assembled and the role of gas dissipation affect the correlation (or lack of) between M_{BH} and σ or L . Simulations of mergers of gas-rich disk galaxies are able to produce remnant galaxies that follow the observed $M_{\text{BH}} - \sigma$ correlation in Figure 3a, over an intermediate range of $M_{\text{BH}} \sim 10^7 - 10^9 M_{\odot}$.^{19,20} By contrast, simulations of major mergers of gas-poor elliptical galaxies, which are a likely path to forming the most massive galaxies, show that mergers with low-angular momentum progenitor orbits could increase M_{BH} and L by similar numerical factors without increasing the velocity dispersion²¹. The correlation between M_{BH} and σ may therefore steepen or disappear altogether at the high end. Massive elliptical galaxies retain residual quantities of gas even after the decline of star formation. Accretion of this gas onto the galaxies' central black holes could help grow M_{BH} and further steepen the $M_{\text{BH}} - \sigma$ and $M_{\text{BH}} - L$ relations.

Black holes in excess of $10^{10} M_{\odot}$ are observed as quasars in the early Universe, from 1.4 to 3.3 billion years after the Big Bang ($z = 2 - 4.5$). Throughout the last 10.4 billion years, however, these extremely massive black holes have been dormant, and the average mass of the black holes powering quasars has decreased steadily¹. Quasar activity and elliptical galaxy formation are predicted to arise from similar merger-triggered processes, and there is growing evidence that present-day massive ellipticals once hosted the most luminous high-redshift quasars²². Yet definitive classification of these quasars' host galaxies has remained elusive.

Our measurements of black holes with nearly $10^{10} M_{\odot}$ in NGC 3842 and NGC 4889 provide circumstantial evidence that BCGs host the remnants of extremely luminous quasars. Further insight can be gained by comparing the number density of nearby BCGs ($\sim 5 \times 10^{-6} \text{ Mpc}^{-3}$) to the present-day number density of black holes inferred from the number densities, duty cycles, and black hole masses of quasars. Quasar-based predictions for the number density of black holes with mass between 10^9 and $10^{10} M_{\odot}$ agree with the predicted black hole number density ($\sim 3 \times 10^{-7}$ to 10^{-5} Mpc^{-3}) from combining the $M_{\text{BH}} - L$ relation with the luminosity function of nearby galaxies. The predicted number density from the $M_{\text{BH}} - \sigma$ relation, however, is an order of magnitude less than the inferred quasar population^{16,23}. The two predictions can be reconciled if the $M_{\text{BH}} - \sigma$ relation has upward curvature or a large degree of intrinsic

scatter in M_{BH} at the high-mass end, as suggested by our new measurements. With improvements in adaptive optics instrumentation on large optical telescopes and very-long baseline interferometry at radio wavelengths, black holes are being sought and detected in increasingly exotic host galaxies. Along with our measurements of the black hole masses in NGC 3842 and NGC 4889, future measurements in other BCGs will quantify the cumulative growth of supermassive black holes in the Universe's densest environments.

References

1. Vestergaard, H., Fan, X., Tremonti, C. A., Osmer, P. S. & Richards, G. T. Mass functions of the active black holes in distant quasars from the Sloan Digital Sky Survey data release 3. *Astrophys. J.* **674**, L1-L4 (2008).
2. Sargent, W. L. W., *et al.* Dynamical evidence for a central mass concentration in the galaxy M87. *Astrophys. J.* **221**, 731-744 (1978).
3. Gebhardt, K., *et al.* The black hole mass in M87 from Gemini/NIFS adaptive optics observations. *Astrophys. J.* **729**, 119 (2011).
4. Dressler, A. Observational evidence for supermassive black holes. In D. E. Osterbrock, & J. S. Miller (ed.) *Dark Matter in Galaxies*, vol. 134 of *IAU Symposium*, 217 (1989).
5. Kormendy, J. & Richstone, D. Inward bound the search for supermassive black holes in galactic nuclei. *Ann. Rev. Astron. Astrophys.* **33**, 581-624 (1995).
6. Ferrarese, L. & Merritt, D. A fundamental relation between supermassive black holes and their host galaxies. *Astrophys. J.* **539**, L9-L12 (2000).
7. Gebhardt, K., *et al.* A relationship between nuclear black hole mass and galaxy velocity dispersion. *Astrophys. J.* **539**, L13-L16 (2000).
8. Gültekin, K., *et al.* The $M_{\text{BH}} - \sigma$ and $M_{\text{BH}} - L$ relations in galactic bulges, and determinations of their intrinsic scatter. *Astrophys. J.* **698**, 198-221 (2009).
9. Allington-Smith, J., *et al.* Integral field spectroscopy with the Gemini Multi-Object Spectrograph. I. Design, construction, and testing. *Pub. Astron. Soc. Pacific* **115**, 892-912 (2002).
10. Larkin, J., *et al.* OSIRIS: a diffraction limited integral field spectrograph for Keck. *Proc. Soc. Photo-optical Instrumentation Engineers* **6269**, 62691A (2006).
11. Hill, G. J., *et al.* Design, construction, and performance of VIRUS-P: the prototype of a highly replicated integral field spectrograph for the HET. *Proc. Soc. Photo-optical Instrumentation Engineers* **7014**, 701470 (2008).
12. Laine, S., *et al.* Hubble Space Telescope imaging of brightest cluster galaxies. *Astron. J.* **125**, 478-505 (2003).
13. Postman, M. & Lauer, T. R. Brightest cluster galaxies as standard candles. *Astrophys. J.* **440**, 28-47 (1995).
14. Schwarzschild, M. A numerical model for a triaxial stellar system in dynamical equilibrium. *Astrophys. J.* **232**, 236-247 (1979).
15. Loubser, S. I., Sansom, A. E., Sánchez-Blázquez, P., Soechting, I. K. & Bromage, G. E., Radial kinematics of brightest cluster galaxies. *Mon. Not. R. Astron. Soc.* **391**, 1009-1028 (2008).
16. Lauer, T. R., *et al.* The masses of nuclear black holes in luminous elliptical galaxies and implications for the space density of the most massive black holes. *Astrophys. J.* **662**, 808-834 (2007).
17. Dalla Bontà, E., *et al.* The high-mass end of the black hole mass function: mass estimates in brightest cluster galaxies. *Astrophys. J.* **690**, 537-559 (2009).
18. Nowak, N., *et al.* The supermassive black hole of Fornax A. *Mon. Not. R. Astron. Soc.* **391**, 1629-1649 (2008).
19. Di Matteo, T., Volker, S., & Hernquist, L. Energy input from quasars regulates the growth and activity of black holes and their host galaxies *Nature* **433**, 604-607 (2005).
20. Robertson, B., *et al.* The Evolution of the $M_{\text{BH}} - \sigma$ Relation. *Astrophys. J.* **641**, 90-102 (2006).
21. Boylan-Kolchin, M., Ma, C.-P., & Quataert, E. Red mergers and the assembly of massive elliptical galaxies: the fundamental plane and its projections. *Mon. Not. R. Astron. Soc.* **369**, 1081-1089 (2006).
22. Hopkins, P. F., Bundy, K., Hernquist, L. & Ellis, R. S. Observational evidence for the coevolution of galaxy mergers, quasars, and the blue/red galaxy transition. *Astrophys. J.* **659**, 976-996 (2007).
23. Lauer, T. R., Tremaine, S., Richstone, D., & Faber, S. M. Selection bias in observing the cosmological evolution of the $M_{\text{BH}} - \sigma$ and $M_{\text{BH}} - L$ relationships. *Astrophys. J.* **670**, 249-260 (2007).

Supplementary Information is linked to the online version of the paper at <http://www.nature.com/nature>.

Acknowledgments N.J.M. and K.G. are supported by the National Science Foundation. C.-P.M. is supported by NASA and by the Miller Institute for Basic Research in Science, University of California, Berkeley. S.A.W. is supported by NASA through the Hubble Fellowship. Data presented here were obtained using Gemini Observatory, W.M. Keck Observatory, and McDonald Observatory. Gemini is operated by the Association of Universities for Research in Astronomy, Inc., under a cooperative agreement with the NSF on behalf of the Gemini partnership. The W. M. Keck Observatory is operated as a scientific partnership among the California Institute of Technology, the University of California, and the National Aeronautics and Space Administration. McDonald Observatory is operated by the University of Texas at Austin. Stellar orbit models were run using the facilities at the Texas Advanced Computing Center at The University of Texas at Austin.

Author Contributions N.J.M. carried out the data analysis and modeling for this paper and wrote most of the text. C.-P.M. and S.A.W. contributed significant portions of the text, and C.-P.M. compiled the data for Figure 3 and oversaw communication among all the co-authors. S.A.W. analyzed OSIRIS data of NGC 3842. K.G. provided GMOS data of NGC 3842 and NGC 4889. K.G. and D.O.R. developed the stellar orbit modeling code. J.D.M. provided VIRUS-P data of NGC 3842. T.R.L. provided photometric data and image analysis of NGC 3842 and NGC 4889. J.R.G. led the OSIRIS observing campaign for NGC 3842. All authors contributed to the interpretive analysis of the observations and the writing of the paper.

Competing Interests The authors declare that they have no competing financial interests.

Correspondence Correspondence and requests for materials should be addressed to N. McConnell (email: nmcc@berkeley.edu) or C.-P. Ma (cpma@berkeley.edu).

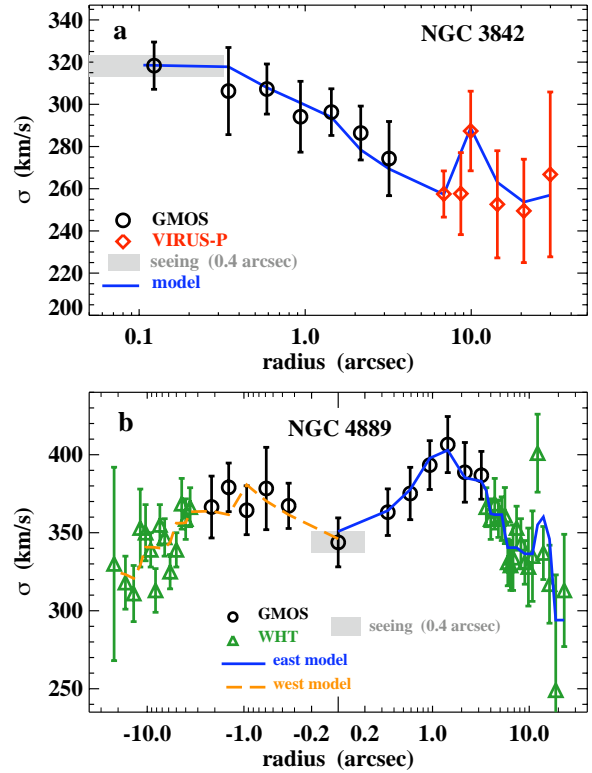


Figure 2 | One-dimensional profiles of the line-of-sight velocity dispersions, σ , in NGC 3842 and NGC 4889. **(a)** Dispersion versus radius in NGC 3842, after averaging data from 0° to 180° with respect to the major axis. Black circles represent measurements from GMOS, and red diamonds represent measurements from VIRUS-P. The solid blue line is the projected line-of-sight dispersion from our best-fitting stellar orbit model of NGC 3842. **(b)** Dispersion versus radius along the major axis of NGC 4889. Black circles represent measurements from GMOS, and green triangles represent measurements from WHT¹⁵. The maximum velocity dispersion occurs 1.4 arcseconds east of the galaxy center ($r = +1.4''$). The solid blue line is the projected line-of-sight dispersion from our best-fitting orbit model using data from the east side of NGC 4889 ($r > 0$). The dashed orange line is the velocity dispersion from our best-fitting orbit model using data from the west side of NGC 4889 ($r < 0$). Error bars in both plots represent 1 standard deviation.

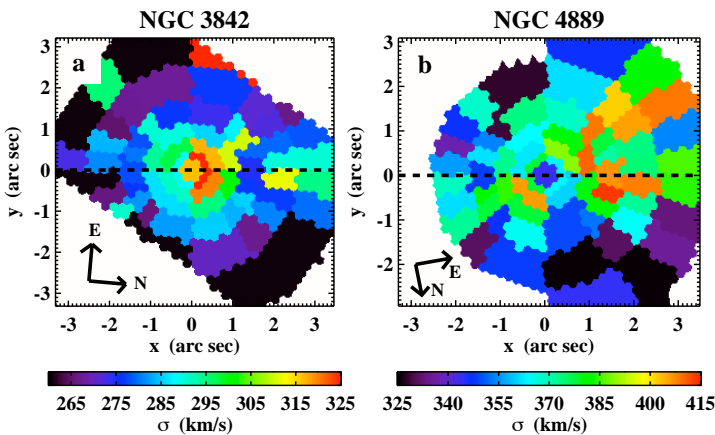


Figure 1 | Two-dimensional maps of the line-of-sight stellar velocity dispersions, σ , of the central regions of NGC 3842 and NGC 4889. **(a)** In NGC 3842, a $9.7 \times 10^9 M_\odot$ black hole is responsible for the increase in σ toward the galaxy center. **(b)** In NGC 4889, the highest velocity dispersions, near 410 km s^{-1} , are located on the east side of the galaxy, at least 1.1 arcseconds from the center. The horizontal dashed line in each panel traces the major axis of the galaxy.

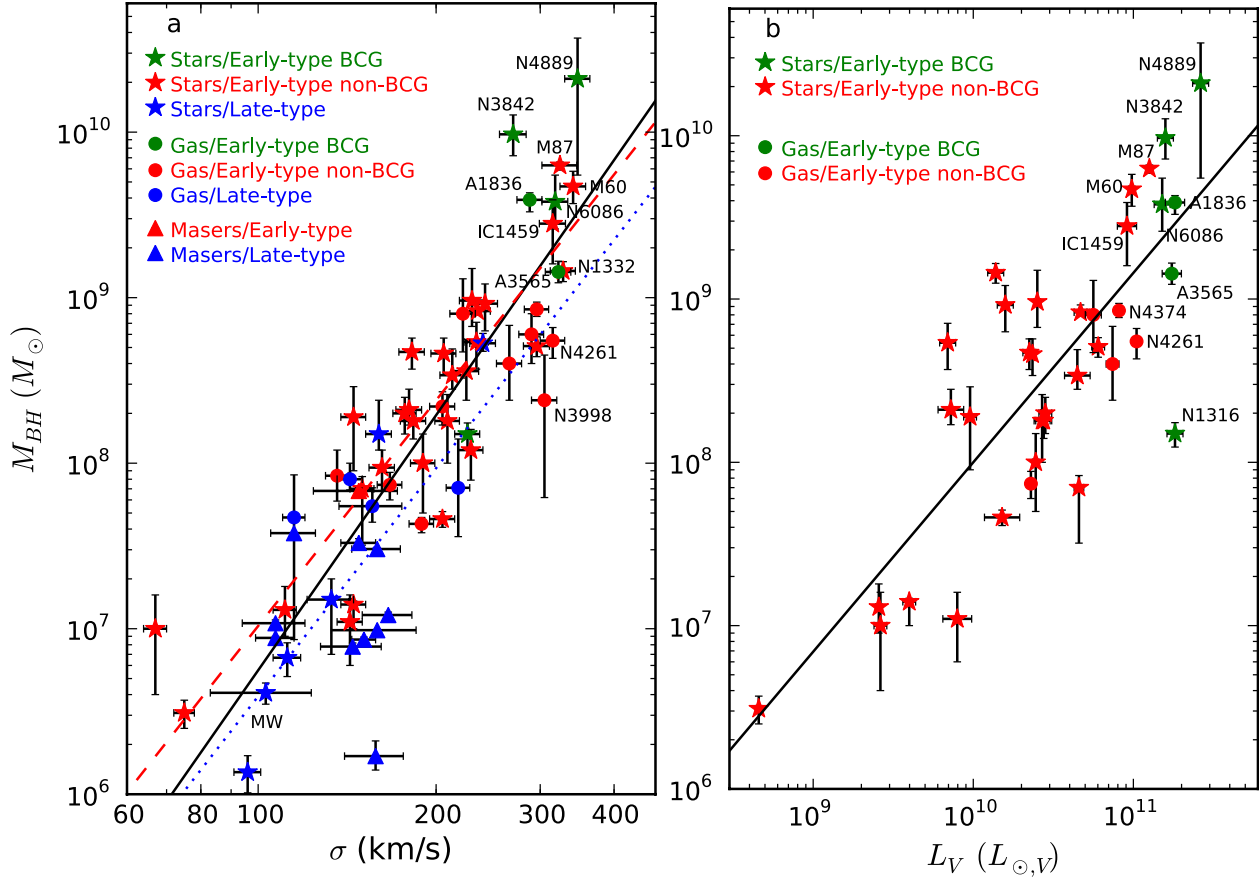


Figure 3 | Empirical relations between the central black hole masses and bulk properties of galaxies. **(a)** Black hole mass, M_{BH} , versus stellar velocity dispersion, σ , for 65 galaxies with direct dynamical measurements of M_{BH} . For galaxies with available data, σ is the luminosity-weighted average within one effective radius. Our sample includes 32 measurements from a 2009 compilation⁸, 16 galaxies with updated masses since 2009, 15 new galaxies with M_{BH} measurements, and the two galaxies reported here. A complete list of the galaxies is given in Table 3 of Supplementary Information. Brightest cluster galaxies (BCGs; defined here as the most luminous galaxy in a cluster) are plotted in green, other elliptical and S0 galaxies are plotted in red, and late-type spiral galaxies are plotted in blue. Stars represent galaxies whose black holes were measured using stellar dynamics, circles represent gas-dynamical measurements, and triangles represent maser-based measurements. Error bars represent 68% confidence intervals. For most of the maser galaxies, the error bars in M_{BH} are smaller than the plotted triangle symbol. The solid black line illustrates the best-fit power law for the entire sample: $\log_{10}(M_{\text{BH}}/M_{\odot}) = 8.29 + 5.12 \log_{10}(\sigma/200 \text{ km s}^{-1})$. When early-type and late-type galaxies are fit separately, the resulting power laws are $\log_{10}(M_{\text{BH}}/M_{\odot}) = 8.83 + 4.53 \log_{10}(\sigma/200 \text{ km s}^{-1})$ for elliptical and S0 galaxies (dashed red line), and $\log_{10}(M_{\text{BH}}/M_{\odot}) = 7.97 + 4.58 \log_{10}(\sigma/200 \text{ km s}^{-1})$ for spiral galaxies (dotted blue line). We do not label M87 as a BCG, as is commonly done, as NGC 4472 in the Virgo cluster is 0.2 magnitudes brighter. **(b)** Black hole mass versus V-band bulge luminosity, L_V , for 36 early-type galaxies with direct dynamical measurements of M_{BH} . The solid black line illustrates the best-fit power law for the entire sample: $\log_{10}(M_{\text{BH}}/M_{\odot}) = 9.16 + 1.16 \log_{10}(L_V/10^{11} L_{\odot})$.

Supplementary Information

Spectroscopic Data and LOSVD Extraction

We map stellar orbital motions in NGC 3842 and NGC 4889 by measuring the line-of-sight velocity distribution (LOSVD) for different regions in each galaxy. Each LOSVD is determined by fitting a composite template stellar spectrum to a fully reduced spectrum of the galaxy. The LOSVDs are non-parametric probability distributions, defined at each of 15 velocity bins. We use a Maximum Penalized Likelihood technique to optimize the LOSVD value in each velocity bin while simultaneously optimizing the weights of individual template stars^{18,24,25}.

In Table 1, we summarize our observations with the integral field spectrographs GMOS, OSIRIS, and VIRUS-P. Figures 4-6 illustrate a sample galaxy and template spectrum from each instrument. Our data from GMOS only cover radii within 3.8 arcseconds (1.8 kpc) of the center of NGC 3842 and NGC 4889, and by themselves cannot fully remove the degeneracies between M_{BH} and M_*/L . For NGC 3842, our VIRUS-P measurements cover radii out to 35.3 arcseconds (16.8 kpc) and can distinguish the enclosed stellar mass profile from the galaxy’s dark matter halo. This allows for an accurate determination of M_*/L , such that the GMOS data can accurately constrain M_{BH} . At radii from 3.6 to 23.0 arcseconds (1.8 – 11.5 kpc) along the major axis of NGC 4889, we use Gaussian velocity profiles from Loubser et al. (2008)¹⁵.

Our GMOS spectra for NGC 3842 and NGC 4889 are centered on the calcium triplet absorption lines near 860 nm. A sample GMOS spectrum for each galaxy is shown in Figure 4, demonstrating the clean line profiles that are typical for this spectral region. Another advantage to using the calcium triplet is that kinematic measurements are not highly sensitive to the stellar template used²⁶.

OSIRIS data of NGC 3842 were acquired with the 0.05 arcsecond spatial scale and the broad *H*-band filter, which spans a large number of atomic and molecular absorption features. To measure kinematics, we fit carbon monoxide band heads at 1598, 1619, 1640, and 1661 nm, and a deep magnesium feature near 1500 nm. The most severe source of noise in our OSIRIS spectra is residual narrow-line emission from the night sky. This background emission varies rapidly and is only partially corrected by recording 15-minute sky frames in between pairs of 15-minute science exposures. Even when masked, the contaminated channels represent a non-negligible loss of spectral information. This must be countered by increasing the signal-to-noise ratio in the usable parts of the spectrum. To achieve adequate signal-to-noise, we bin the data to the same spatial regions as the overlapping LOSVDs from GMOS. Each of the final bins contains approximately 80 OSIRIS spatial pixels.

VIRUS-P data were acquired in low-resolution mode, which provides broad wavelength coverage. The poorest instrumental resolution over our field is 0.56 nm full width at half-maximum (FWHM), which is adequate considering that stellar velocity dispersions in NGC 3842 are typically near 250 km s^{-1} , corresponding to a resolution of approximately $0.7 \text{ nm FWHM} \times (\lambda / 360 \text{ nm})$. We fit VIRUS-P spectra with 16 template stars from the Indo-US library²⁷, spanning spectral types from B9 to M3 and including stars with sub-solar and super-solar metallicities. However, some spectral regions require additional adjustments to account for metallicities and elemental abundance ratios outside the range of our template library. We do not attempt to fit the entire spectral range simultaneously, but instead follow the same fitting procedure used by Murphy et al. (2011)²⁸ for VIRUS-P data of M87. Each spectrum is divided into four sub-regions, as illustrated in Figure 6. We independently determine the best-fit LOSVD for each sub-region and discard any sub-regions that fail to produce a believable fit. We then average the LOSVDs derived from individual spectral sub-regions.

Our stellar orbit models are axisymmetric, and so each of our final LOSVDs must represent an average over four quadrants of the galaxy. In order to preserve any rotational signal along the major axis, we invert the

velocities from LOSVDs on the south side of NGC 3842 and the west side of NGC 4889. However, neither galaxy shows strong rotation. In NGC 3842, the resulting kinematics are sufficiently symmetric to average the LOSVDs from opposite sides of the galaxy. In NGC 4889, we have modeled four quadrants of the galaxy independently.

Our stellar orbit models require an estimate of the point spread function (PSF) for each instrument at the time of spectroscopic observations. We estimate the PSF for our GMOS data for both NGC 3842 and NGC 4889 from wide-field images taken during target acquisition. Although the models discussed herein assume a 0.4-arcsecond PSF for GMOS data, we have run a small number of models with a 0.7-arcsecond PSF and have found no significant changes in our results. While observing NGC 3842, we switched from the OSIRIS spectrograph to the OSIRIS imaging camera every few hours, and observed the adaptive optics tip/tilt star. We can tolerate a large degree of uncertainty in our measured PSF, as we have rebinned OSIRIS data of NGC 3842 to spatial scales that are several times coarser than the diffraction-limited FWHM.

Photometric Data

Our stellar orbit models are constrained to reproduce the observed stellar light profile of each galaxy, which requires accurate measurements of each galaxy’s surface brightness profile over a large radial range. For radii out to 10 arcseconds, we adopt high-resolution *I*-band (800 nm) surface brightness profiles, obtained with WFPC2 on the Hubble Space Telescope, and deconvolved with the instrumental PSF¹². At larger radii out to 115 arcseconds, we use *R*-band (600 nm) data obtained with the 2.1 m telescope at Kitt Peak National Observatory (KPNO). The KPNO data have a field of view of 5.2×5.2 arcminutes, which enables accurate sky subtraction. We combine the individual profiles from WFPC2 and KPNO data at overlapping radii between 5 and 10 arcseconds, accounting for the average *R* – *I* color over these radii. To compute the luminosity density profile of each galaxy, we deproject the surface brightness profile while assuming spheroidal isodensity contours²⁹.

Stellar Orbit Models and Statistical Analysis

We generate models of NGC 3842 and NGC 4889 using Schwarzschild’s method¹⁴, in which test particle orbits are computed in a static axisymmetric gravitational potential. We assume that each galaxy contains three mass components: stars, a central black hole, and an extended dark matter halo. The stellar mass density is assumed to follow the same profile as the observed luminosity density, with a constant stellar mass-to-light ratio, M_*/L . Our modeling procedures are similar to those for NGC 6086, described in McConnell et al. (2011)³⁰.

Each orbit in the model is assigned a scalar weight, and the set of best-fit orbital weights is determined by comparing projected LOSVDs from the orbits to the observed LOSVDs for the galaxy. Each observed LOSVD spatially maps to a linear combination of bins within the model, according to the spatial boundaries of the corresponding spectrum and the PSF of the observations. A corresponding model LOSVD is computed from the projected velocity distributions of individual orbits in each spatial bin, the appropriate combination of spatial bins, and the orbital weights. The best-fit weights are determined by the method of maximum entropy³¹, with the fixed constraint that the summed spatial distribution of all weighted orbits must match the observed luminosity density profile. The essential output of each model is a measurement of χ^2 , which defines the goodness of fit between our observed LOSVDs and the model LOSVDs, using the optimal combination of orbital weights. We determine the best-fit values and confidence intervals in M_{BH} and M_*/L by evaluating the relative likelihood between models with different assumed values of M_{BH} and M_*/L . Figure 7 illustrates the behavior of χ^2 with respect to M_{BH} and M_*/L , for models with our best fitting dark matter halo.

Kinematic Data from Different Instruments

Stellar kinematics along the major axes of NGC 3842 and NGC 4889 were previously measured by Loubser et al. (2008)¹⁵, using the ISIS long-slit spectrograph on the William Herschel Telescope (WHT). In order to directly compare our GMOS measurements to this earlier investigation, we rebinned our integral-field spectra to match the spatial sampling and slit width of the WHT data. The resulting comparisons for NGC 3842 and NGC 4889 are shown in Figures 8 and 9, respectively. The GMOS and WHT measurements are in good agreement for $r \leq 3.0$ arcseconds in NGC 3842 and for $r \leq 1.6$ arcseconds in NGC 4889. In particular, both data sets reveal that stellar velocity dispersions on the east side of NGC 4889 rise above the central value. We detect a significantly sharper decrease in central velocity dispersion with GMOS, which is consistent with the superior seeing conditions of our data (0.4 arcseconds for GMOS, versus 1.0 arcseconds for WHT). Similarly, the GMOS data reveal a sharper central increase in velocity dispersion for NGC 3842. However, the general consistency between our kinematics and the independent measurements by Loubser et al. indicates that our kinematic extraction method has low systematic errors.

For N3842, our VIRUS-P measurements are also consistent with WHT measurements, which extend along the major axis to $r = 20.8$ arcseconds. We prefer using data from VIRUS-P in our stellar orbit models because they extend to larger radii and provide full two-dimensional spatial sampling.

Near the center of NGC 3842, OSIRIS and GMOS provide independent measurements of stellar kinematics. We have binned data from OSIRIS and GMOS at identical spatial scales out to $r = 0.7$ arcseconds (330 pc) and have run orbit models fitting LOSVDs from OSIRIS and GMOS simultaneously (as well as VIRUS-P data at large radii). Including the OSIRIS data causes the best-fit value of M_{BH} to decrease by up to 23%, and the best-fit value of M_{\star}/L to increase by as much as 8%. This occurs because OSIRIS data show a less drastic increase in velocity dispersion than data from GMOS. In spite of these differences, results with and without OSIRIS data are consistent at the 68% confidence level.

Models fitting OSIRIS and GMOS data together yield higher average χ^2 values per LOSVD. This is true even if we ignore the central regions where LOSVDs from OSIRIS and GMOS are not fully consistent. Even with several template stars, the overlapping absorption features in the H-band spectral region are difficult to model, and the LOSVDs derived from OSIRIS data may have systematic errors. Consequently, we judge the models with only GMOS and VIRUS-P data to be more reliable.

Models of NGC 4889

Stellar kinematics in NGC 4889 are asymmetric with respect to the major and minor axes of the galaxy. Integral-field data from GMOS reveals velocity dispersions above 410 km s^{-1} on the east side of the galaxy, while the velocity dispersion rarely exceeds 380 km s^{-1} on the west side. This asymmetry prevents NGC 4889 from being fully described by a single set of axisymmetric orbit models. In order to place upper and lower bounds on the central black hole mass, we have run four suites of models, each fitting kinematics from one projected quadrant of NGC 4889. The northeast, southeast, and northwest quadrants yield consistent black hole masses, spanning a 68% confidence interval of $M_{\text{BH}} = 1.0 - 3.7 \times 10^{10} M_{\odot}$. The southwest quadrant has a maximum velocity dispersion of 373 km/s and yields a 68% confidence interval of $M_{\text{BH}} = 0.6 - 1.7 \times 10^{10} M_{\odot}$.

We have run an additional set of models to approximate M_{BH} in the case of an off-center black hole. We apply a constant spatial offset of 1.4 arcseconds (700 pc) to the kinematics on the east side of the galaxy, such that the highest velocity dispersion is aligned with the center of the model gravitational potential. These models cannot be fully trusted because the kinematic and photometric data are misaligned. Still, the resulting 68% confidence interval for M_{BH} falls entirely within the range bracketed by the models from different quadrants. Results from individual trials are

listed in Table 2. Figure 10 illustrates χ^2 versus M_{BH} for each series of models, after marginalizing over M_{\star}/L .

The individual quadrants of NGC 4889 represent large variations in stellar kinematics, but each quadrant still partially constrains the enclosed mass within the central few arcseconds. By adopting the most extreme range of confidence limits, $M_{\text{BH}} = 0.6 - 3.7 \times 10^{10} M_{\odot}$, we only exclude black holes whose gravitational influence would contradict our entire field of data. Further extensions to this confidence interval should only reflect overall systematic biases. Large systematic biases in our kinematic measurements are unlikely, as demonstrated by their agreement with independent measurements by Loubser et al. (2008)¹⁵. Our models of NGC 4889 assume an edge-on inclination. This is indirectly supported by the observed axis ratio of 0.7, which implies a relatively eccentric intrinsic shape even for an edge-on system. Models with a more face-on inclination might yield a systematically higher black hole mass³². A fundamental assumption of all orbit superposition models is that the stellar motions reflect a steady-state gravitational potential, rather than transient conditions. These models could misrepresent the range of allowed black hole masses if the observed kinematics in NGC 4889 reflected a temporary phenomenon such as an ongoing galaxy merger. NGC 4889 appears photometrically undisturbed, reducing the likelihood of such an event.

Because our adopted confidence interval places large error bars on M_{BH} in NGC 4889, this galaxy has relatively little weight in our fits to the $M_{\text{BH}} - \sigma$ and $M_{\text{BH}} - L$ relationships. A systematic error in our measurement would produce a minimal bias in the best-fit relations. Likewise, our discussion of steepening and scatter at the high-mass ends of the correlations depends upon several objects and is not highly sensitive to the measurement in NGC 4889.

Power-Law Fits to the $M_{\text{BH}} - \sigma$ and $M_{\text{BH}} - L$ Relations

We revisit the $M_{\text{BH}} - \sigma$ and $M_{\text{BH}} - L$ relations by updating the sample of 49 black holes from Gültekin et al. (2009; hereafter G09)⁸, which was compiled from earlier studies. Including NGC 3842 and NGC 4889, we add 17 galaxies with recently measured black hole masses to the sample. The new objects include two more BCGs^{18,30}, eight active galactic nuclei with high-precision maser-based measurements^{33,34}, and two galaxies with pseudobulges³⁵. We also include updated black hole masses for 16 other galaxies in the 2009 sample, based on stellar orbit models with dark matter halos and more thorough orbit libraries^{3,32,36,37}. In particular, the revised masses for M60 and M87 are twice as large as the earlier values.

Our updated sample uses the same selection criteria as G09; in particular, only direct dynamical measurements of M_{BH} are included. G09 estimated galaxy distances by assuming a Hubble parameter $H_0 = 70 \text{ km s}^{-1} \text{ Mpc}^{-1}$, and rescaled their sample of black hole masses accordingly ($M_{\text{BH}} \propto D$). We have followed this convention for NGC 3842, NGC 4889, and the rest of our sample. Our fits to $M_{\text{BH}}(\sigma)$ do not include upper limits. Updated models of one galaxy, NGC 2778, do not produce a significant black hole detection; after removing this object, our updated sample contains 65 black hole masses.

We define σ in the same manner as the 2009 sample. Wherever possible, we use the luminosity-weighted effective velocity dispersion, measured using spatially resolved data out to one effective radius. G09 found no evidence of systematic bias between this definition of σ and more ubiquitous single-aperture measurements. Nonetheless, several galaxies in G09 have measurements of σ that include data at very small radii, within which the central black hole directly influences the stellar velocity dispersion. This is inappropriate for studies that wish to treat M_{BH} and σ as fundamentally independent variables. We have therefore re-evaluated σ in three galaxies with large black hole masses and available spatially resolved kinematics, by excluding data within the black hole's radius of influence. We use this same treatment to measure σ for NGC 3842 and NGC 4889. For M87, we adopt the updated values of M_{BH} and σ from Gebhardt et al. (2011)³. Following G09, we assume all measurements of σ have an un-

certainty of at least 5%.

To fit the $M_{\text{BH}} - L$ relationship, we only consider early-type galaxies for which the stellar luminosity of the spheroidal component can be measured reliably. Including NGC 3842, we add 6 galaxies to the $M_{\text{BH}} - L$ sample of G09. We exclude NGC 2778. We also exclude NGC 3607 and NGC 4564, for which the literature contains large discrepancies in the measured luminosity^{8,16}. Our final sample for fitting $M_{\text{BH}} - L$ contains 36 black hole masses.

Our fits to $M_{\text{BH}} - \sigma$ and $M_{\text{BH}} - L$ assume a single-index power law as the functional form of both relations, following the convention most commonly used in prior studies. Specifically, we define the $M_{\text{BH}} - \sigma$ relationship to be $\log_{10}(M_{\text{BH}}/M_{\odot}) = \alpha + \beta \log_{10}(\sigma/200 \text{ km s}^{-1})$, and the $M_{\text{BH}} - L$ relationship to be $\log_{10}(M_{\text{BH}}/M_{\odot}) = \alpha + \beta \log_{10}(L_V/10^{11} L_{\odot})$. For each relationship, we follow the method of Tremaine et al. (2002)³⁸ to fit for α and β . We minimize the quantity

$$\chi^2 = \sum_{i=1}^N \frac{(M_{\text{BH},i} - \alpha - \beta \sigma_i)^2}{\epsilon_0^2 + \epsilon_{M,i}^2 + \beta^2 \epsilon_{\sigma,i}^2} \quad (1)$$

where ϵ_{σ} is the measurement error in σ , ϵ_M is the measurement error in M_{BH} , and ϵ_0 is the intrinsic scatter in the $M_{\text{BH}} - \sigma$ relation. We set ϵ_0 such that χ^2 per degree of freedom is unity after minimization. The 68% confidence intervals for α and β correspond to the maximum range of α and β for which $\chi^2 - \chi_{\text{min}}^2 \leq 1$.

We list our best-fit values of α , β , and ϵ_0 for various sub-samples in Table 3. We list our full sample of galaxies in Table 4.

References

24. Gebhardt, K., *et al.* Axisymmetric, three-integral models of galaxies: a massive black hole in NGC 3379. *Astron. J.* **119**, 1157-1171 (2000).

25. Pinkney, J., *et al.* Kinematics of 10 early-type galaxies from Hubble Space Telescope and ground-based spectroscopy. *Astrophys. J.* **596**, 903-929 (2003).

26. Barth, A. J., Ho, L. C., & Sargent, W. L. W. A study of the direct fitting method for measurement of galaxy velocity dispersions. *Astron. J.* **124**, 2607-2614 (2002).

27. Valdes, F., Gupta, R., Rose, J. A., Singh, H. P., & Bell, D. J. The Indo-US library of Coudé feed stellar spectra. *Astrophys. J. Supp.* **152**, 251-259 (2004).

28. Murphy, J. D., Gebhardt, K., & Adams, J. J., Galaxy kinematics with VIRUS-P: the dark matter halo of M87. *Astrophys. J.* **729**, 129 (2011).

29. Gebhardt, K., *et al.* The centers of early-type galaxies with HST. III. Non-parametric recovery of stellar luminosity distribution. *Astron. J.* **112**, 105-113 (1996).

30. McConnell, N. J., *et al.* The black hole mass in brightest cluster galaxy NGC 6086. *Astrophys. J.* **728**, 100 (2011).

31. Richstone, D. O., & Tremaine, S. Maximum-entropy models of galaxies. *Astrophys. J.* **327**, 82-88 (1988).

32. van den Bosch, R. C. E. & de Zeeuw, P. T. Estimating black hole masses in triaxial galaxies. *Mon. Not. R. Astron. Soc.* **401**, 1770-1780 (2010).

33. Greene, J. E., *et al.* Precise black hole masses from megamaser disks: black hole-bulge relations at low mass. *Astrophys. J.* **721**, 26-45 (2010).

34. Kuo, C. Y., *et al.* The megamaser cosmology project. III. Accurate masses of seven supermassive black holes in active galaxies with circumnuclear megamaser disks. *Astrophys. J.* **727**, 20 (2011).

35. Kormendy, J., Bender, R., & Cornell, M. E. Supermassive black holes do not correlate with galaxy disks or pseudobulges. *Nature* **469**, 74-76 (2011).

36. Shen, J. & Gebhardt, K. The supermassive black hole and dark matter halo of NGC 4649 (M60). *Astrophys. J.* **711**, 484-494 (2010).

37. Schulze, A. & Gebhardt, K. Effect of a dark matter halo on the determination of black hole masses. *Astrophys. J.* **729**, 21 (2011).

38. Tremaine, S., *et al.* The slope of the black hole mass versus velocity dispersion correlation. *Astrophys. J.* **574**, 740-753 (2002).

39. Ghez, A. M., *et al.* Measuring distance and properties of the Milky Way's central supermassive black hole with stellar orbits. *Astrophys. J.* **689**, 1044-1062 (2008).

40. Gillessen, S., *et al.* Monitoring stellar orbits around the massive black hole in the galactic center. *Astrophys. J.* **692**, 1075-1109 (2009).

41. Greenhill, L. J., *et al.* A warped accretion disk and wide-angle outflow in the inner parsec of the Circinus galaxy. *Astrophys. J.* **590**, 162-173 (2003).

42. Cappellari, M., *et al.* The counterrotating core and the black hole mass of IC 1459. *Astrophys. J.* **578**, 787-805 (2002).

43. Verolme, E. K., *et al.* A SAURON study of M32: measuring the intrinsic flattening and the central black hole mass. *Mon. Not. R. Astron. Soc.* **335**, 517-525 (2002).

44. Bender, R., *et al.* HST STIS spectroscopy of the triple nucleus of M31: two nested disks in Keplerian rotation around a supermassive black hole. *Astrophys. J.* **631**, 280-300 (2005).

45. Krajnovic, D., McDermid, R. M., Cappellari, M., & Davies, R. L. Determination of masses of the central black holes in NGC 524 and 2549 using laser guide star adaptive optics. *Mon. Not. R. Astron. Soc.* **399**, 1839-1857 (2009).

46. Bower, G. A., *et al.* Evidence of a supermassive black hole in the galaxy NGC 1023 from nuclear stellar dynamics. *Astrophys. J.* **550**, 75-86 (2001).

47. Lodato, G. & Bertin, G. Non-Keplerian rotation in the nucleus of NGC 1068: evidence for a massive accretion disk?. *Astron. Astrophys.* **398**, 517-524 (2003).

48. Atkinson, J. W., *et al.* Supermassive black hole mass measurements for NGC 1300 and 2748 based on Hubble Space Telescope emission-line gas kinematics. *Mon. Not. R. Astron. Soc.* **359**, 504-520 (2005).

49. Rusli, S. P., *et al.* The central black hole mass of the high- σ but low-bulge-luminosity lenticular galaxy NGC 1332. *Mon. Not. R. Astron. Soc.* **410**, 1223-1236 (2011).

50. Gebhardt, K., *et al.* The black hole mass and extreme orbital structure in NGC 1399. *Astrophys. J.* **671**, 1321-1328 (2007).

51. Houghton, R. C. W., *et al.* The central kinematics of NGC 1399 measured with 14 pc resolution. *Mon. Not. R. Astron. Soc.* **367**, 2-18 (2006).

52. Sarzi, M., *et al.* Supermassive black holes in bulges. *Astrophys. J.* **550**, 65-74 (2001).

53. Devereux, N., Ford, H., Tsvetanov, Z., & Jacoby, G. STIS spectroscopy of the central 10 parsecs of M81: evidence for a massive black hole. *Astron. J.* **125**, 1226-1235 (2003).

54. Emsellem, E., Dejonghe, H., & Bacon, R. Dynamical models of NGC 3115. *Mon. Not. R. Astron. Soc.* **303**, 495-514 (1999).

55. Davies, R. L., *et al.* The star-forming torus and stellar dynamical black hole mass in the Seyfert 1 nucleus of NGC 3227. *Astrophys. J.* **646**, 754-773 (2006).

56. Barth, A. J., *et al.* Evidence for a supermassive black hole in the S0 galaxy NGC 3245. *Astrophys. J.* **555**, 685-708 (2001).

57. Kondratko, P. T., Greenhill, L. J., & Moran, J. M. The parsec-scale accretion disk in NGC 3393. *Astrophys. J.* **678**, 87-95 (2008).

58. Gültekin, K., *et al.* A quintet of black hole mass determinations. *Astrophys. J.* **695**, 1577-1590 (2009).

59. de Francesco, G., Capetti, A., & Marconi, A. Measuring supermassive black holes with gas kinematics: the active S0 galaxy NGC 3998. *Astron. Astrophys.* **460**, 439-448 (2006).

60. Herrnstein, J. R., Moran, J. M., Greenhill, L. J., & Trotter, A. S. The geometry of and mass accretion rate through the maser accretion disk in NGC 4258. *Astrophys. J.* **429**, 719-738 (2005).

61. Ferrarese, L. & Ford, H. C. Nuclear disks of gas and dust in early-type galaxies and the hunt for massive black holes: Hubble Space Telescope observations of NGC 6251. *Astrophys. J.* **515**, 583-602 (1996).

62. Cretton, N. & van den Bosch, F. C. Evidence for a massive black hole in the S0 galaxy NGC 4342. *Astrophys. J.* **514**, 704-724 (1999).

63. Walsh, J. L., Barth, A. J., & Sarzi, M. The supermassive black hole in M84 revisited. *Astrophys. J.* **721**, 762-776 (2010).

64. Nowak, N., *et al.* The supermassive black hole in NGC 4486A detected with SINFONI at the Very Large Telescope. *Mon. Not. R. Astron. Soc.* **379**, 909-914 (2007).

65. de Francesco, G., Capetti, A., & Marconi, A. Measuring supermassive black holes with gas kinematics. II. The LINERs IC 989, NGC 5077, and NGC 6500. *Astron. Astrophys.* **479**, 355-363 (2008).

66. Silge, J. D., Gebhardt, K., Bergmann, M., & Richstone, D. Gemini Near Infrared Spectrograph observations of the central supermassive black hole in Centaurus A. *Astron. J.* **130**, 406-417 (2005).

67. Cappellari, M., *et al.* The mass of the black hole in Centaurus A from SINFONI AO-assisted integral-field observations of stellar kinematics. *Mon. Not. R. Astron. Soc.* **394**, 660-674 (2009).

68. Ferrarese, L., Ford, H. C., & Jaffe, W. Evidence for a massive black hole in the active galaxy NGC 4261 from Hubble Space Telescope images and spectra. *Astrophys. J.* **470**, 444-459 (1999).

69. van der Marel, R. P., & van den Bosch, F. C. Evidence for a $3 \times 10^8 M_{\odot}$ black hole in NGC 7052 from Hubble Space Telescope observations of the nuclear gas disk. *Astron. J.* **116**, 2220-2236 (1998).

70. Wold, M., Lacy, M., Käuff, H. U., & Siebenmorgen, R. The nuclear regions of NGC 7582 from [Ne II] spectroscopy at $12.8 \mu\text{m}$ - an estimate of the black hole mass. *Astron. Astrophys.* **460**, 449-457 (2006).

71. Braatz, J. A., *et al.* The megamaser cosmology project. II. The angular-diameter distance to UGC 3789. *Astrophys. J.* **718**, 657-665 (2010).

72. Graham, A. W., Colless, M. M., Busarello, G., Zaggia, S., & Longo, G. Extended stellar kinematics of elliptical galaxies in the Fornax cluster. *Astron. Astrophys. Supp.* **133**, 325-336 (1998).

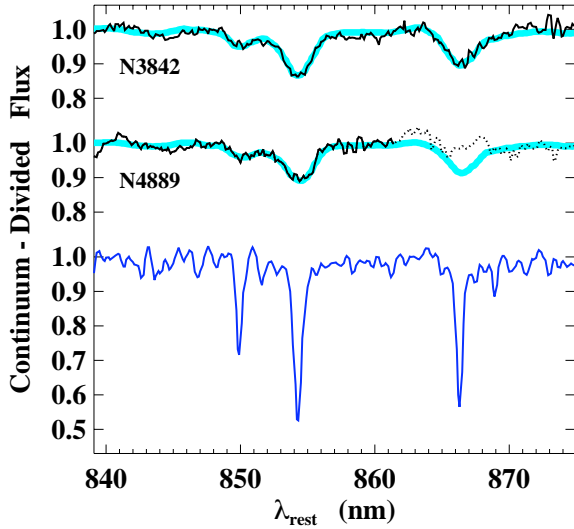


Figure 4 | GMOS spectra of NGC 3842 and NGC 4889. Each spectrum corresponds to the center of the galaxy ($r < 0.25$ arcseconds). The upper spectrum is NGC 3842 (black), overlaid with the best-fitting, LOSVD-convolved template spectrum (thick, light blue). The middle spectrum is NGC 4889, overlaid with the best-fitting template spectrum. The dotted portion of the spectrum was excluded from the LOSVD fitting. The lower spectrum is template star HD 73710 (G9III), before convolution with the LOSVD.

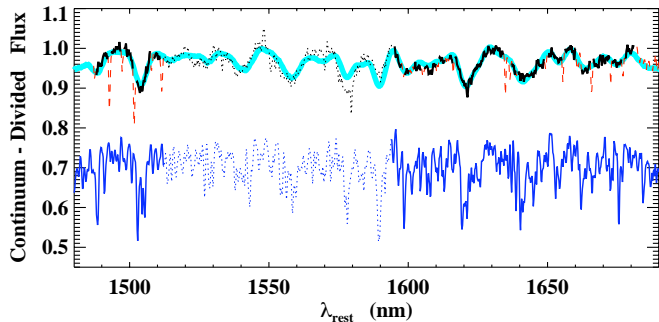


Figure 5 | OSIRIS spectrum of the central region of NGC 3842 ($r < 0.25$ arcseconds, or 110 pc). The upper spectrum is NGC 3842 (black), overlaid with the best-fitting, LOSVD-convolved template spectrum (thick, light blue). The red dashed lines in the galaxy spectrum are residuals from imperfectly subtracted sky emission. The lower spectrum is the best-fit composite template before convolution with the LOSVD. Our observed template stars fit spectra of NGC 3842 poorly across the dotted region from 1510 to 1590 nm, and therefore this region is excluded from kinematic fitting.

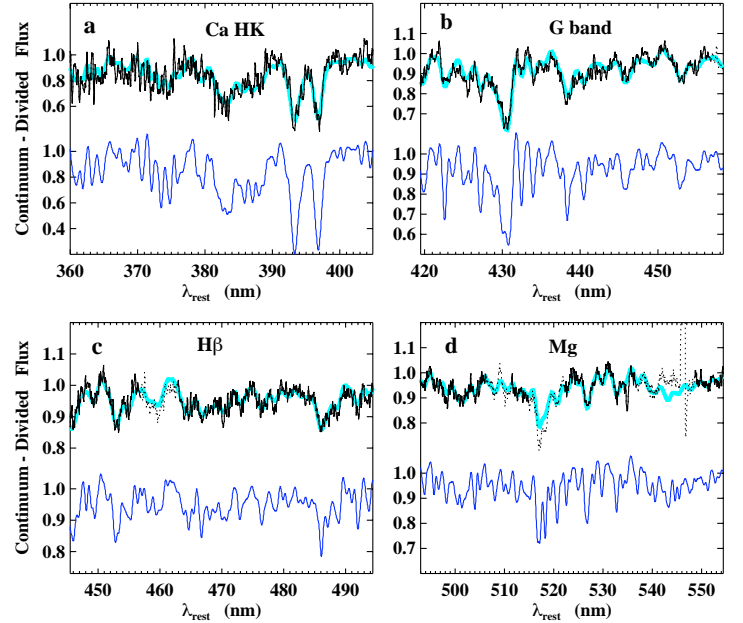


Figure 6 | VIRUS-P spectrum of NGC 3842, corresponding to a semi-annulus with an inner radius of 17.0 arcseconds (7.7 kpc) and an outer radius of 24.5 arcseconds (11.0 kpc). The four panels contain different sub-regions of the galaxy spectrum. Each sub-region is evaluated independently for a best-fit LOSVD and best-fit composite template spectrum. The upper spectrum in each panel is NGC 3842 (black), overlaid with the best-fitting, LOSVD-convolved template spectrum (thick, light blue). Dotted portions of the galaxy spectrum have been masked from the fit. The lower spectrum in each panel is the best-fit composite template before convolution with the LOSVD.

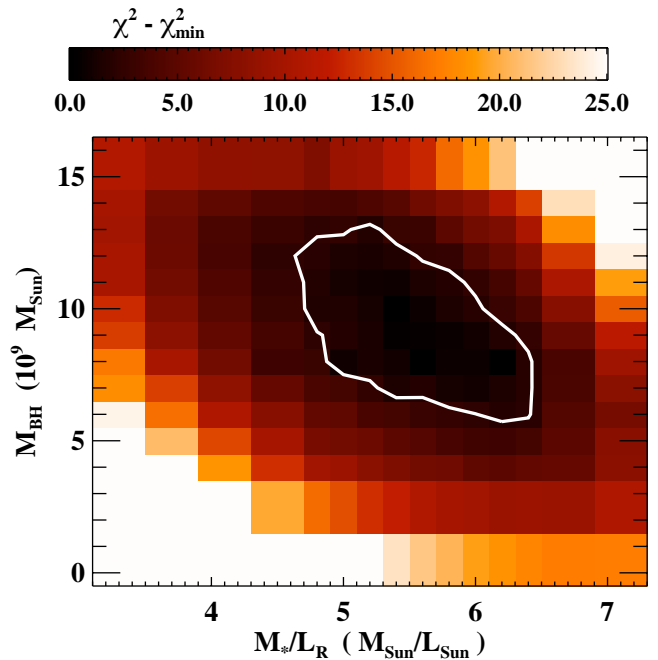


Figure 7 | Map of χ^2 versus M_{BH} and M_*/L for stellar orbit models of NGC 3842. The models fit data from GMOS and VIRUS-P. The diagonal trend in χ^2 indicates the degeneracy between stellar mass and black hole mass near the center of NGC 3842. For two free parameters with Gaussian likelihood distributions, the 68% confidence interval is defined where $\chi^2 - \chi^2_{\text{min}} \leq 2.30$, illustrated by the thick white contour. We obtain 68% confidence intervals of $6.812.0 \times 10^9 M_\odot$ for M_{BH} , and $4.66.1 M_\odot/L_\odot$ for M_*/L . The median values, which we adopt as our final measurements, are $M_{\text{BH}} = 9.2 \times 10^9 M_\odot$ and $M_*/L = 5.4 M_\odot/L_\odot$.

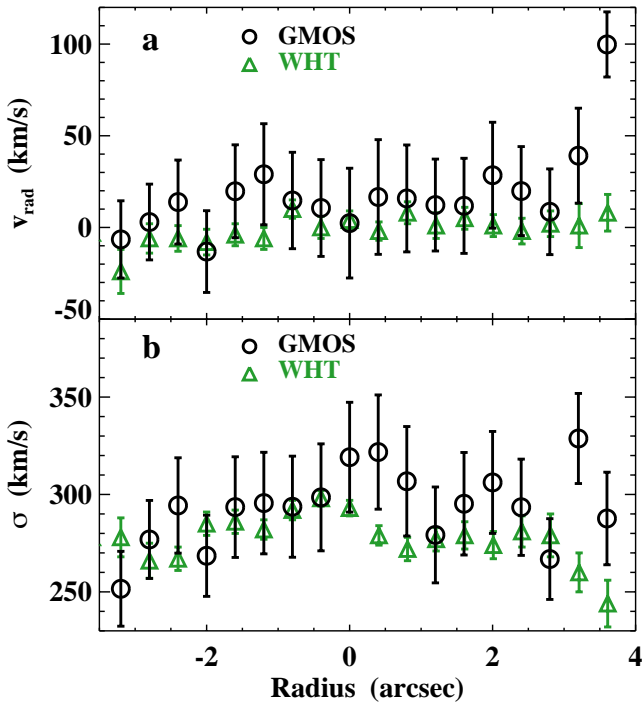


Figure 8 | (a) Radial velocity vs. radius in NGC 3842. Green triangles are measurements from Loubser et al. (2008)¹⁵, using the ISIS spectrograph on the William Herschel Telescope (WHT). Black circles are measurements from the GMOS integral-field unit, after rebinning to match the spatial sampling of the WHT data. Plotted error bars represent 1 standard deviation; the GMOS and WHT measurements agree within errors. (b) Velocity dispersion vs. radius for NGC 3842. The velocity dispersion measurements from GMOS and WHT agree for $r < 3$ arcseconds, except for two points near the galaxy center. Measurements from GMOS show a steeper increase in velocity dispersion, consistent with the relative seeing between the two observations (0.4 arcseconds for GMOS, versus 1.0 arcseconds for WHT).

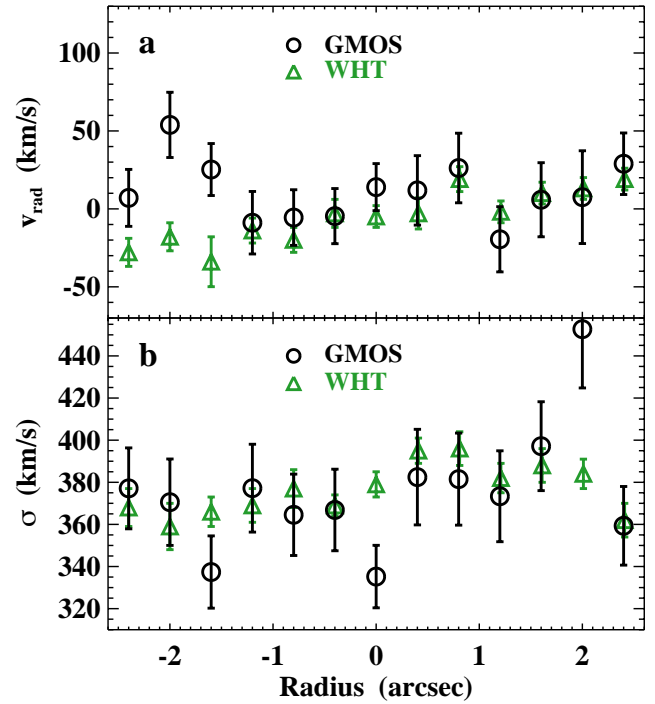


Figure 9 | (a) Radial velocity vs. radius in NGC 4889. Green triangles are measurements from Loubser et al. (2008)¹⁵, using the ISIS spectrograph on the William Herschel Telescope (WHT). Black circles are measurements from the GMOS integral-field unit, after rebinning to match the spatial sampling of the WHT data. Error bars represent 1 standard deviation. At radii from 1.2 arcseconds on the west side to 2.4 arcseconds on the east side, the GMOS and WHT measurements agree within errors. (b) Velocity dispersion vs. radius for NGC 4889. The velocity dispersion measurements from GMOS and WHT agree from 1.2 arcseconds on the west side to 1.6 arcseconds on the east side. The central measurement from GMOS shows a sharp decrease in velocity dispersion, which might be unresolved in the WHT data due to worse seeing (1.0 arcseconds).

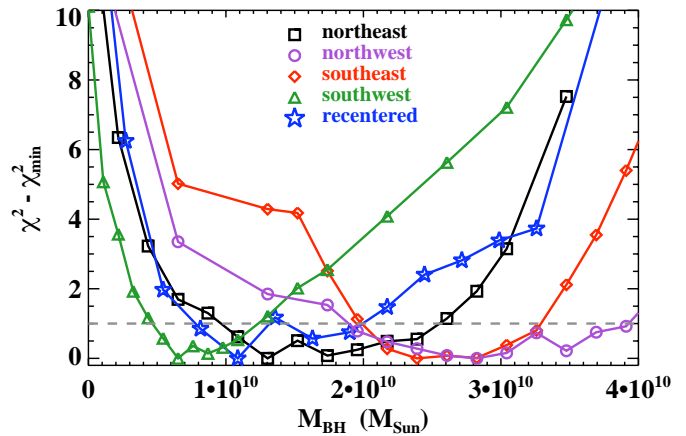


Figure 10 | χ^2 vs. M_{BH} for NGC 4889, after marginalizing over M_*/L . Each line with symbols represents a models constrained by different set of LOSVDs from GMOS. Black squares, purple circles, red diamonds, and green triangles each use LOSVDs from a different quadrant of the galaxy. Blue stars represent models with spatially offset LOSVDs, to match the largest velocity dispersion with the center of the gravitational potential. Considering all models, the 68% confidence interval for M_{BH} is $0.6 - 3.7 \times 10^{10} M_{\odot}$.

Table 1 | Spectroscopic observations

Galaxy	Instrument	UT Date	N_{exp}	t_{exp} (s)	λ (nm)	$\Delta\lambda$ (nm)	r_{max} (arcsec)	Δr (arcsec)	PSF FWHM (arc sec)
NGC 3842	GMOS	April 27, 2003	5	1200	755-949	0.25	3.8	0.2	0.4
NGC 3842	OSIRIS	May 8-10, 2010	16	900	1473-1803	0.72	0.7	0.05	0.08
NGC 3842	VIRUS-P	March 7-8, 2011	3	1200	358-589	0.52	35.3	4.1	2.0
NGC 4889	GMOS	March 13, 2003	5	1200	755-949	0.25	3.8	0.2	0.4

Notes: N_{exp} is the number of science exposures recorded. t_{exp} is the integration time per exposure. $\Delta\lambda$ is the median instrumental resolution (FWHM). r_{max} is the maximum radius of usable data, with respect to the center of the galaxy. Δr is the instrumental spatial scale, equal to the angular diameter of one lenslet or fiber.

Table 2 | Models of NGC 4889

Quadrant	M_{BH} (M_{\odot})	$M_{\text{BH},\text{min}}$ (M_{\odot})	$M_{\text{BH},\text{max}}$ (M_{\odot})	M_{\star}/L (M_{\odot}/L_{\odot})	M_{\star}/L_{min} (M_{\odot}/L_{\odot})	M_{\star}/L_{max} (M_{\odot}/L_{\odot})
northeast	1.7×10^{10}	1.0×10^{10}	2.5×10^{10}	6.1	4.6	7.3
southeast	2.6×10^{10}	2.0×10^{10}	3.2×10^{10}	5.6	4.2	6.7
northwest	2.7×10^{10}	1.6×10^{10}	3.7×10^{10}	5.8	4.4	7.0
southwest	9.8×10^9	5.5×10^9	1.7×10^{10}	6.6	5.3	7.6
east	2.9×10^{10}	2.1×10^{10}	3.4×10^{10}	5.4	4.5	6.4
west	1.2×10^{10}	6.5×10^9	2.0×10^{10}	6.4	5.2	7.4
recentered	1.5×10^{10}	8.7×10^9	2.4×10^{10}	6.5	5.4	7.3

Notes: The “east” and “west” trials used LOSVDs from spectra that were binned symmetrically over the north and south sides of the galaxy. The “re-centered” trial added an artificial position offset to the LOSVDs, such that the maximum velocity dispersion was placed at the center of the gravitational potential. $M_{\text{BH},\text{min}}$, $M_{\text{BH},\text{max}}$, M_{\star}/L_{min} , and M_{\star}/L_{max} represent 68% confidence limits. M_{\star}/L corresponds to R -band photometry.

Table 3 | Fits to $M_{\text{BH}} - \sigma$ and $M_{\text{BH}} - L$

Relationship	Sample	N_{gal}	α	β	ϵ_0
$M_{\text{BH}} - \sigma$	all	65	8.29 ± 0.06	5.12 ± 0.36	0.43
$M_{\text{BH}} - \sigma$	early-type	45	8.38 ± 0.06	4.53 ± 0.40	0.38
$M_{\text{BH}} - \sigma$	late-type	20	7.97 ± 0.22	4.58 ± 1.25	0.47
$M_{\text{BH}} - \sigma$	ML	36	8.43 ± 0.07	4.66 ± 0.43	0.38
$M_{\text{BH}} - L$	ML	36	9.16 ± 0.11	1.16 ± 0.14	0.50

Notes: N_{gal} is the number of galaxies in the sample. ML refers to the sample of early-type galaxies with reliable spheroid luminosity measurements.

Table 4 | Galaxies with dynamical measurements of M_{BH}

Galaxy	Type	D	σ	$\log_{10}(L_{V,\text{sph}})$	M_{BH}	$M_{\text{BH,min}}$	$M_{\text{BH,max}}$	Method	Ref.
		(Mpc)	(km s^{-1})	$\log_{10}(L_{\odot})$	(M_{\odot})	(M_{\odot})	(M_{\odot})		
Milky Way ^a	Sbc	0.008	103 ± 20		4.1 × 10 ⁶	3.5 × 10 ⁶	4.7 × 10 ⁶	stars	8,39,40
A1836-BCG	E	157.5	288 ± 14	11.26	3.9 × 10 ⁹	3.3 × 10 ⁹	4.3 × 10 ⁹	gas	8,17
A3565-BCG ^b	E	54.4	322 ± 16	11.24	1.4 × 10 ⁹	1.2 × 10 ⁹	1.7 × 10 ⁹	gas	17
Circinus	Sb	4.0	158 ± 18		1.7 × 10 ⁶	1.4 × 10 ⁶	2.1 × 10 ⁶	masers	8,41
IC1459 ^c	E4	30.9	315 ± 16	10.96	2.8 × 10 ⁹	1.6 × 10 ⁹	3.9 × 10 ⁹	stars	8,42
N221 (M32)	E2	0.86	75 ± 3	8.66	3.1 × 10 ⁶	2.5 × 10 ⁶	3.7 × 10 ⁶	stars	8,43
N224 (M31)	Sb	0.80	160 ± 8		1.5 × 10 ⁸	1.2 × 10 ⁸	2.4 × 10 ⁸	stars	8,44
N524	S0	23.3	235 ± 12	10.67	8.3 × 10 ⁸	7.9 × 10 ⁸	9.2 × 10 ⁸	stars	45
N821	E4	25.5	209 ± 10	10.43	1.8 × 10 ⁸	1.0 × 10 ⁸	2.6 × 10 ⁸	stars	37
N1023	SB0	12.1	205 ± 10	10.18	14.6 × 10 ⁷	4.1 × 10 ⁷	5.1 × 10 ⁷	stars	8,46
N1068 (M77)	SB	15.4	151 ± 7		8.6 × 10 ⁶	8.3 × 10 ⁶	8.9 × 10 ⁶	masers	8,47
N1194 ^{b,d}	SA0+	55.5	148 ⁺²⁶ ₋₂₂		6.8 × 10 ⁷	6.5 × 10 ⁷	7.1 × 10 ⁷	masers	34
N1300	SB(rs)bc	20.1	218 ± 10		7.1 × 10 ⁷	3.6 × 10 ⁷	1.4 × 10 ⁸	gas	8,48
N1316	E	18.6	226 ± 11	11.26	1.5 × 10 ⁸	1.24 × 10 ⁸	1.75 × 10 ⁸	stars	18
N1332	S0	22.3	328 ± 16	10.14	1.45 × 10 ⁹	1.25 × 10 ⁹	1.65 × 10 ⁹	stars	49
N1399 ^{e,f}	E1	21.1	296 ± 15	10.78	5.1 × 10 ⁸	4.4 × 10 ⁸	5.8 × 10 ⁸	stars	8,50
N1399 ^{e,f}	E1	21.1	296 ± 15	10.78	1.3 × 10 ⁹	6.4 × 10 ⁸	1.8 × 10 ⁹	stars	8,51
N2273 ^{b,d}	SB(r)a	26.8	144 ⁺¹⁸ ₋₁₆		7.8 × 10 ⁶	7.4 × 10 ⁶	8.2 × 10 ⁶	masers	34
N2549	S0	12.3	145 ± 7	9.60	1.4 × 10 ⁷	1.0 × 10 ⁷	1.47 × 10 ⁷	stars	45
N2748	Sc	24.9	115 ± 5		4.7 × 10 ⁷	8.6 × 10 ⁶	8.5 × 10 ⁷	gas	8,48
N2787	SB0	7.9	189 ± 9		4.3 × 10 ⁷	3.8 × 10 ⁷	4.7 × 10 ⁷	gas	8,52
N2960 ^{b,d}	Sa	75.3	166 ⁺¹⁶ ₋₁₅		1.21 × 10 ⁷	1.16 × 10 ⁷	1.26 × 10 ⁷	masers	34
N3031 (M81)	Sb	4.1	143 ± 7		8.0 × 10 ⁷	6.9 × 10 ⁷	1.0 × 10 ⁸	gas	8,53
N3115	S0	10.2	230 ± 11	10.40	9.6 × 10 ⁸	6.7 × 10 ⁸	1.5 × 10 ⁹	stars	8,54
N3227	SBa	17.0	133 ± 12		1.5 × 10 ⁷	7.0 × 10 ⁶	2.0 × 10 ⁷	stars	8,55
N3245	S0	22.1	205 ± 10		2.2 × 10 ⁸	1.7 × 10 ⁸	2.7 × 10 ⁸	gas	8,56
N3377	E6	11.7	145 ± 7	9.98	1.9 × 10 ⁸	9.0 × 10 ⁷	2.9 × 10 ⁸	stars	37
N3379 (M105) ^b	E0	11.7	206 ± 10	10.37	4.6 × 10 ⁸	3.4 × 10 ⁸	5.7 × 10 ⁸	stars	32
N3384	E1	11.7	143 ± 7	9.90	1.1 × 10 ⁷	6.0 × 10 ⁶	1.6 × 10 ⁷	stars	37
N3393 ^b	SB(rs)	53.6	148 ± 10		3.3 × 10 ⁷	3.1 × 10 ⁷	3.5 × 10 ⁷	masers	57
N3585	S0	21.2	213 ± 10	10.65	3.4 × 10 ⁸	2.8 × 10 ⁸	4.9 × 10 ⁸	stars	8,58
N3607 ^g	E1	19.9	229 ± 11		1.2 × 10 ⁸	7.9 × 10 ⁷	1.6 × 10 ⁸	stars	8,58
N3608	E1	23.0	182 ± 9	10.35	4.7 × 10 ⁸	3.7 × 10 ⁸	5.7 × 10 ⁸	stars	37
N3842 ^h	E	98.4	270 ± 14	11.20	9.7 × 10 ⁹	7.2 × 10 ⁹	1.27 × 10 ¹⁰	stars	
N3998	S0	14.9	305 ± 15		2.4 × 10 ⁸	6.2 × 10 ⁷	4.5 × 10 ⁸	gas	8,59
N4026	S0	15.6	180 ± 9	9.86	2.1 × 10 ⁸	1.7 × 10 ⁸	2.8 × 10 ⁸	stars	8,58
N4258	SABbc	7.2	115 ± 10		3.78 × 10 ⁷	3.77 × 10 ⁷	3.79 × 10 ⁷	masers	8,60
N4261	E2	33.4	315 ± 15	11.02	5.5 × 10 ⁸	4.3 × 10 ⁸	6.6 × 10 ⁸	gas	8,61
N4291	E2	25.0	242 ± 12	10.20	9.2 × 10 ⁸	6.3 × 10 ⁸	1.21 × 10 ⁹	stars	37
N4342	S0	18.0	225 ± 11		3.6 × 10 ⁸	2.4 × 10 ⁸	5.6 × 10 ⁸	stars	8,62
N4374 (M84)	E1	17.0	296 ± 14	10.91	8.5 × 10 ⁸	7.7 × 10 ⁸	9.4 × 10 ⁸	gas	63
N4388 ^{b,d}	SA(s)b	19.8	107 ⁺⁸ ₋₇		8.8 × 10 ⁶	8.6 × 10 ⁶	9.0 × 10 ⁶	masers	34
N4459	E2	17.0	167 ± 8	10.36	7.4 × 10 ⁷	6.0 × 10 ⁷	8.8 × 10 ⁷	gas	8,52
N4473	E4	17.0	190 ± 9	10.39	1.0 × 10 ⁸	5.0 × 10 ⁷	1.5 × 10 ⁸	stars	37
N4486 (M87) ^{b,i}	E1	17.0	324 ⁺²⁸ ₋₁₆	11.10	6.3 × 10 ⁹	5.9 × 10 ⁹	6.6 × 10 ⁹	stars	3
N4486A	E2	17.0	111 ± 5	9.41	1.3 × 10 ⁷	9.0 × 10 ⁶	1.8 × 10 ⁷	stars	8,64
N4564 ^j	S0	17.0	162 ± 8		9.4 × 10 ⁷	6.8 × 10 ⁷	1.2 × 10 ⁸	stars	37
N4594 (M104)	Sa	10.3	240 ± 12		5.3 × 10 ⁸	4.74 × 10 ⁸	6.08 × 10 ⁸	stars	35
N4596	SB0	18.0	136 ± 6		8.4 × 10 ⁷	5.9 × 10 ⁷	1.2 × 10 ⁸	gas	8,52
N4649 (M60) ^{b,k}	E2	16.5	341 ± 17	10.99	4.7 × 10 ⁹	3.7 × 10 ⁹	5.8 × 10 ⁹	stars	36

Continued on next page.

Table 3, continued

Galaxy	Type	D	σ	$\log_{10}(L_{V,\text{sph}})$	M_{BH}	$M_{\text{BH},\text{min}}$	$M_{\text{BH},\text{max}}$	Method	Ref.
		(Mpc)	(km s ⁻¹)	$\log_{10}(L_{\odot})$	(M _⊙)	(M _⊙)	(M _⊙)		
N4697	E6	12.4	177 ± 8	10.45	2.0 × 10 ⁸	1.8 × 10 ⁸	2.2 × 10 ⁸	stars	37
N4736 (M94)	Sab	4.9	112 ± 6		6.68 × 10 ⁶	5.14 × 10 ⁶	8.22 × 10 ⁶	stars	35
N4826 (M64)	Sab	6.4	96 ± 5		1.36 × 10 ⁶	1.02 × 10 ⁶	1.71 × 10 ⁶	stars	35
N4889 ^l	E	103.2	347 ± 17	11.42	2.1 × 10 ¹⁰	5.5 × 10 ⁹	3.7 × 10 ¹⁰	stars	
N5077	E3	44.9	222 ± 11	10.75	8.0 × 10 ⁸	4.7 × 10 ⁸	1.3 × 10 ⁹	gas	8,65
N5128 ^e	S0/E	4.4	150 ± 7	10.66	3.0 × 10 ⁸	2.8 × 10 ⁸	3.4 × 10 ⁸	stars	8,66
N5128 ^e	S0/E	4.4	150 ± 7	10.66	7.0 × 10 ⁷	3.2 × 10 ⁷	8.3 × 10 ⁷	stars	8,67
N5576	E3	27.1	183 ± 9	10.44	1.8 × 10 ⁸	1.4 × 10 ⁸	2.1 × 10 ⁸	stars	8,58
N5845	E3	28.7	234 ± 11	9.84	5.4 × 10 ⁸	3.7 × 10 ⁸	7.1 × 10 ⁸	stars	37
N6086 ^b	E	139.1	318 ± 16	11.18	3.8 × 10 ⁹	2.6 × 10 ⁹	5.5 × 10 ⁹	stars	30
N6251	E1	106.0	290 ± 14		6.0 × 10 ⁸	4.0 × 10 ⁸	8.0 × 10 ⁸	gas	8,68
N6264 ^{b,d}	S	145.4	158 ⁺¹⁵ ₋₁₄		3.03 × 10 ⁷	2.99 × 10 ⁷	3.08 × 10 ⁷	masers	34
N6323 ^{b,d}	Sab	110.5	158 ⁺²⁸ ₋₂₃		9.8 × 10 ⁶	9.7 × 10 ⁶	9.9 × 10 ⁶	masers	34
N7052	E3	70.9	266 ± 13	10.87	4.0 × 10 ⁸	2.4 × 10 ⁸	6.8 × 10 ⁸	gas	8,69
N7457	S0	14.0	67 ± 3	9.42	1.0 × 10 ⁷	4.0 × 10 ⁶	1.6 × 10 ⁷	stars	37
N7582	SBab	22.3	156 ± 19		5.5 × 10 ⁷	4.4 × 10 ⁷	7.1 × 10 ⁷	gas	8,70
U3789 ^{b,d}	SA(r)ab	48.4	107 ⁺¹³ ₋₁₂		1.08 × 10 ⁷	1.03 × 10 ⁷	1.14 × 10 ⁷	masers	34

Notes: D is the distance to the galaxy, assuming $H_0 = 70 \text{ km s}^{-1} \text{ Mpc}^{-1}$. $L_{V,\text{sph}}$ is the V -band stellar luminosity of the galaxy's spheroidal component. $M_{\text{BH},\text{min}}$ and $M_{\text{BH},\text{max}}$ are the upper and lower bounds of the 68% confidence interval in M_{BH} .

^a The literature contains a large number of estimates for the velocity dispersion of our Galaxy's bulge, using different kinematic tracers at different radii. We use the radially averaged measurement of $\sigma = 103 \pm 20 \text{ km s}^{-1}$ from Tremaine et al. (2002)³⁸.

^b G09 use the convention $H_0 = 70 \text{ km s}^{-1} \text{ Mpc}^{-1}$ for all galaxies whose distances are derived from systemic velocity measurements. To match this convention, we have adjusted the distance to several galaxies in our updated sample. All distance adjustments yield corresponding adjustments to M_{BH} , $M_{\text{BH},\text{min}}$, and $M_{\text{BH},\text{max}}$, such that $M_{\text{BH}} \propto D$. Our reported 68% confidence intervals for M_{BH} do not include uncertainties in the distance measurements.

^c We derive an effective velocity dispersion of 315 km s^{-1} for IC 1459, using spatially resolved major-axis kinematics from Cappellari et al. (2002)⁴², at radii of 0.8 - 25.1 arcseconds. For $r < 0.8$ arcseconds, stellar motions are directly influenced by the central black hole.

^d Maser-based black hole masses for several galaxies are presented in Greene et al. (2010)³³ and Kuo et al. (2011)³⁴. We use the velocity dispersions presented in Greene et al. (2010). For consistency with the rest of our sample, we use the black hole masses from Kuo et al. (2011), which agree with the values in Greene et al. (2010) but do not include distance uncertainties in the overall uncertainty for M_{BH} . Braatz et al. (2010)⁷¹ provide an updated distance and black hole mass for UGC 3789, which are consistent with the values we adopt from Kuo et al. (2011).

^e Following G09, our sample includes two distinct measurements for NGC 1399 and also for NGC 5128. We weight each of these measurements by 50% when performing fits to $M_{\text{BH}}(\sigma)$ and $M_{\text{BH}}(L)$. In Figure 3 we only plot the more recent measurement for each galaxy.

^f We derive an effective velocity dispersion of 296 km s^{-1} for NGC 1399, using spatially resolved measurements from Graham et al. (1998)⁷² and Gebhardt et al. (2007)⁵⁰ at radii of 0.6 - 41 arcseconds. For $r < 0.6$ arcseconds, stellar motions are directly influenced by the central black hole.

^g The literature contains two inconsistent estimates of the stellar luminosity in NGC 3607: $M_V = -21.62$ in G09, and $M_V = -19.88$ in Lauer et al. (2007)¹⁶.

^h We derive an effective velocity dispersion of 270 km s^{-1} for NGC 3842, using measurements from GMOS and VIRUS-P at radii of 1.2 - 29.8 arcseconds. For $r < 1.2$ arcseconds, stellar motions are directly influenced by the central black hole.

ⁱ For M87, we use the updated velocity dispersion of 324 km s^{-1} from Gebhardt et al. (2011)³, based on measurements at radii of 2.1 - 100 arcseconds. For $r < 2.1$ arcseconds, stellar motions are directly influenced by the central black hole.

^j The literature contains two inconsistent estimates of the bulge stellar luminosity in NGC 4564: $M_V = -19.60$ in G09, and $M_V = -20.26$ in Lauer et al. (2007)¹⁶.

^k We derive an effective velocity dispersion of 341 km s^{-1} for M60, using spatially resolved measurements from Pinkney et al. (2003)²⁵ at radii of 2.2 - 44 arcseconds. For $r < 2.2$ arcseconds, stellar motions are directly influenced by the central black hole.

^l Our quoted value of M_{BH} for NGC 4889 is the median of the 68% confidence interval $0.7 - 3.4 \times 10^{10} M_{\odot}$. We derive an effective velocity dispersion of 347 km s^{-1} , using kinematics from Loubser et al. (2008)¹⁵ at radii of 2.0 - 22.9 arcseconds. The inner cutoff of 2.0 arcseconds excludes the asymmetric velocity dispersion peak and possible stellar torus.